



Surface and mechanical properties of transparent polycrystalline YAG fabricated by SPS

Paola Palmero, Barbara Bonelli, Gilbert Fantozzi, Giulia Spina, Guillaume Bonnefont, Laura Montanaro, Jérôme Chevalier

► To cite this version:

Paola Palmero, Barbara Bonelli, Gilbert Fantozzi, Giulia Spina, Guillaume Bonnefont, et al.. Surface and mechanical properties of transparent polycrystalline YAG fabricated by SPS. Materials Research Bulletin, 2013, 48 (7), pp.2589-2597. 10.1016/j.materresbull.2013.03.003 . hal-01670836

HAL Id: hal-01670836

<https://hal.science/hal-01670836>

Submitted on 11 Oct 2022

HAL is a multi-disciplinary open access archive for the deposit and dissemination of scientific research documents, whether they are published or not. The documents may come from teaching and research institutions in France or abroad, or from public or private research centers.

L'archive ouverte pluridisciplinaire **HAL**, est destinée au dépôt et à la diffusion de documents scientifiques de niveau recherche, publiés ou non, émanant des établissements d'enseignement et de recherche français ou étrangers, des laboratoires publics ou privés.



Distributed under a Creative Commons Attribution - NonCommercial 4.0 International License

Surface and mechanical properties of transparent polycrystalline YAG fabricated by SPS

P. Palmero ^{a,*}, B. Bonelli ^a, G. Fantozzi ^b, G. Spina ^a, G. Bonnefont ^b, L. Montanaro ^a, J. Chevalier ^b

^a Department of Applied Science and Technology, Politecnico di Torino, INSTM, R.U. PoliTO, LINCE Lab., C.so Duca degli Abruzzi 24, 10129 Torino, Italy

^b Université de Lyon, INSA de Lyon, MATEIS UMR CNRS 5510, Bât. Blaise Pascal, 7 Av. Jean Capelle, 69621 Villeurbanne, France

YAG powder was synthesised by reverse-strike co-precipitation, calcined at 1000 °C and dispersed by either ball-milling with α -alumina (BMA) or zirconia (BMz) spheres or by ultrasonication (US). All the dispersed powders were consolidated by SPS to nearly theoretical density, but only the US powder gave rise to a transparent material (transmittance of about 60% at 600 nm, 1 mm thickness), characterised by an ultra-fine microstructure (average size of 330 nm). In the BM materials, Raman spectroscopy allowed to evidence some phonon vibrational shifts due to secondary phases deriving from pollution by the milling media, not detectable by XRD because present in small amounts. The transmittance of the assintered US sample was further increased by annealing in air at 900 °C; this was assigned to the restoration of some oxygen vacancies created in the reducing environment of the SPS chamber, as evidenced by XPS (X-ray photoelectron spectroscopy). Finally, US samples sintered in the 1250–1400 °C were submitted to a basic mechanical characterisation, showing a very good hardness, in spite of a moderate fracture toughness, especially for the fully dense and fine-grained materials sintered at 1300–1350 °C.

1. Introduction

The polycrystalline yttrium aluminium garnet ($\text{Y}_3\text{Al}_5\text{O}_{12}$, hereafter referred to as YAG) presents outstanding functional and mechanical properties, withstanding high temperatures (melting point of 1940 °C) and corrosive conditions. Its excellent creep behaviour [1], as well as good strength and hardness [2], make YAG suitable as structural ceramic matrix [2] and/or reinforcing phase [3–6], also able to work in harsh environments. When sintered to theoretical density, optically transparent YAG can be yielded, further enlarging its fields of application. Solid-state laser host media, luminous pipes for high-intensity discharge lamps, heat-resistive and armoured windows, IR transparent missile domes are some of the applications where transparent YAG is being used [7–9].

However, densification of polycrystalline YAG to transparency in the visible range is still a challenge process. Generally, it is carried out under vacuum, at very high temperatures and for prolonged time, giving rise to coarsened microstructures [9,10]. In order to limit grain growth and to improve the mechanical

behaviour, spark plasma sintering (SPS) has been already successfully used over the last few years [11,12]. SPS is an emerging consolidation technique which combines pulsed electric current with uniaxial compaction, offering considerable advantages over the conventional sintering routes. In fact, nearly theoretical density can be reached at relatively low sintering temperatures for reduced time, leading to very fine microstructures.

In spite of such advantages, an unavoidable drawback is represented by the carbon contamination in the SPS equipment, limiting the optical performances of the sintered materials [13,14]. Some efforts have been made to limit it: Kim et al. proved the effectiveness of a preheating step in air in increasing the materials transparency [15], whereas Frage et al. demonstrated the cleansing effect of LiF, which reacts with the carbon contaminant giving rise to volatile $(\text{CF})_n$ species, driven off during the SPS cycles [16]. Such reaction also involves the creation of oxygen vacancies, which enhance oxygen diffusivity and promote grain growth, thus annihilating the positive effect of SPS on the final microstructures.

In our previous paper [17], a highly pure YAG powder was synthesised by reverse-strike co-precipitation, calcined at 1000 °C and dispersed by either ball-milling or ultrasonication. Powders derived from both dispersion routes were consolidated by SPS to nearly theoretical density, but only the ultra-sonicated powder gave rise to a transparent material. This sample presented an ultra-fine microstructure (average grain size of 330 nm) containing few, residual small pores and good real in-line transmittance (RIT) in

* Corresponding author at: DISAT (Dipartimento di Scienza Applicata e Tecnologia), Politecnico di Torino, Corso Duca degli Abruzzi, 24, 10129 Torino, Italy. Tel.: +39 011 0904678; fax: +39 011 0904699.

E-mail address: paola.palmero@polito.it (P. Palmero).

both visible and infrared ranges. It was characterised by a greyish colour which turned lighter after annealing in air, further increasing its transparency (66% at 600 nm, for 1 mm thickness).

In spite of these very good results, the measured transmittance values were lower than those expected on the ground of a numerical simulation, which provided the RIT evolution as a function of the pore size, at a given wavelength, sample thickness and residual porosity amount [17]. Thus, with respect to the previous paper, this work intends to deepen whether the carbon contamination and/or oxygen vacancies created in the reducing atmospheres of the SPS chamber during sintering could affect the optical properties of the sintered materials. For this purpose, as-sintered YAG samples as well as materials post-annealed in air at increasing temperatures were submitted to XPS analysis, a useful tool to investigate the influence of oxygen vacancies on the chemical bonding and related energy.

Additionally, the ball-milled and ultra-sonicated materials were analysed by Raman spectroscopy, in order to evidence phonon vibrational shifts by undesired secondary phases, able to affect the YAG transparency. In fact, this spectroscopic technique is an effective tool to investigate the microscopic structure and/or secondary phases segregation as well as the influence of impurities on the lattice vibrational properties of the host materials [18].

Finally, the ultra-sonicated, best performing materials were submitted to a basic mechanical characterisation: Vickers hardness and fracture toughness were determined in materials processed at various SPS temperatures and the results were discussed on the basis of their different microstructural features.

2. Experimental

A pure YAG powder was synthesised by reverse strike co-precipitation, as fully described in some previous papers [17,19–21]. The powder, after calcination at 1000 °C for 30 min, was dispersed under two different conditions [22], precisely by ball-milling and ultrasonication. Ball-milling was carried out by using either α -alumina spheres (mean diameter of 1.5 mm) and tetragonal zirconia spheres (diameter of 2 mm). The powder-to-spheres weight ratio was 1:10 and the solid loading of the slurry was 33 wt.%. About 6 h of ball-milling (in the case of both milling media) and 1 h of ultrasonication were necessary to fully disperse the calcined powder, which reached in all cases a monomodal size distribution, with a mean particle size of about 120 nm [17]. YAG powders dispersed by ultrasonication and by ball-milling, using alumina and zirconia spheres, are hereafter referred to as US, BM_A and BM_Z, respectively.

After being poured into a graphite die of 20 mm in diameter, the dispersed powders were sintered by using a SPS equipment HPD 25/2 (FCT, Germany), under low vacuum (10 Pa) at a constant pressure of 74×10^6 Pa. The SPS cycles were constructed as follows: a fast heating rate (100 °C/min) up to 1100 °C, then a relatively slow heating rate (8 °C/min) up to the sintering temperature, followed by an isothermal step of 15 min. The sintering temperature was varied between 1200 °C and 1400 °C, while all other parameters were kept constant. In particular, the maximum sintering temperature was different for the three powders, and fixed according to the highest final density and optical transmittance obtained. Precisely, it was 1225 °C for BM_A, 1250 °C for BM_Z and 1325 °C for US [17].

Sintered samples were submitted to X-ray diffraction (XRD) spectra were recorded on a Philips PW 1710 apparatus operating with Cu K α radiation (1.541874 Å); spectra were acquired in the range 5–70° 2 θ , with a step size of 0.05° 2 θ and an acquisition time per step of 5 s. Diffraction patterns were indexed by using the Powder Data File database (P.D.F. 2000, International Centre of Diffraction Data, Pennsylvania).

After polishing on both sides up to 1 μ m diamond paste, transparency measurements were performed by using a spectrophotometer UV/Vis NIR V-670 (Jasco, Japan) in the wavelength range from 300 nm to 2500 nm. Transmittance results T_s were recorded on samples of different thicknesses t_s and then normalised to the desired thickness t of 1.5 mm by using the formula:

$$T = T_{th} \left(\frac{T_s}{T_{th}} \right)^{t/t_s}$$

where T_{th} is the YAG theoretical transmittance at a given wavelength, depending on the refractive index n according to:

$$T_{th} = \frac{2n}{n^2 + 1}$$

Different detectors were used inside the spectrophotometer, in the corresponding wavelength range. A PMT detector was used for the UV–vis range, while a Peltier-cooled PbS detector was provided in the NIR region [Jasco specifications].

FE-SEM observations were performed by using a Hitachi S4000 microscope, on both fractured and polished surfaces. Polished samples were submitted to chemical etching, by soaking them in boiling phosphoric acid for 15 s. For each grain size calculation, the dimensions of more than 150 grains were measured.

Subsequent annealing treatments were performed in air, for 1 h, at increasing temperatures, measuring the transmittance after each treatment, in order to follow its evolution as a function of the annealing temperature.

X-ray photoelectron spectroscopy (XPS) was performed on a VersaProbe5000 Physical Electronics X-ray photoelectron spectrometer with a monochromatic Al source and a hemispherical analyser. Survey scans as well as narrow scans (high resolution spectra) were recorded with a 100 μ m spot size on an area of 100 μ m \times 800 μ m spot size. Data acquisition and processing were implemented with the instrument software Summit and MultiPak 8.2. For internal calibration, the XPS spectrometer has been shifted so that the carbon peak lies at 284.60 eV.

Raman spectra were recorded on a Renishaw micro-Raman spectrophotometer using an Ar laser (514.5 nm).

The Vickers micro-hardness was determined on all the samples by applying a maximum load of 500 gf for 15 s, by using a Galileo Microscan instrument. For each indentation, the length of the two diagonals was measured and the corresponding hardness was determined according to standard equations [23]. The mean value of the Vickers hardness was calculated using data from at least 10 clearly readable, not cracked or deformed, indentations.

The fracture toughness (K_{IC}) was estimated by using the Anstis' formula [24]:

$$K_{IC} = A \left(\frac{E}{H} \right)^{1/2} \cdot \frac{P}{c^{3/2}}$$

where A is a geometrical constant, equal to 0.016; E is the Young's modulus, equal to 290 GPa [25]; H is the Vickers hardness; P is the applied load; c is the crack length measured from the centre of indentation to the end of the crack. For each material, at least 5 indentations were evaluated.

3. Results and discussion

3.1. Role of the dispersion route on the optical properties of sintered YAG

The transmittance data and density of BM_Z, BM_A and US sintered materials are collected in Table 1. Though the three samples presented very high final density, the theoretical value

Table 1Fired density, real-in-line transmission (RIT) and average grain size of US, BM_A and BM_Z samples.

Sample/sintering cycle	Fired density (%TD)	RIT at 600 nm for 1.5 mm thickness (% , ± 0.5)	Average grain size (μm)
US/1325 °C-1 h	99.99	52.0	0.330 ± 0.05
BM _A /1225 °C-1 h	99.33	5.6	0.360 ± 0.02
BM _Z /1250 °C-1 h	99.49	1.5	0.380 ± 0.02

was reached only by US ones. Such difference can partially explain the different optical behaviour of the sintered pellets, since a very poor transmittance was shown by both BM samples, whereas a relatively good value was reached for the US material.

Fig. 1 shows the physical appearance of the three samples, placed at about 1 cm over a printed text, confirming their different optical properties. In fact, the printed text is not visible through BM_Z, visible, but not clearly legible, through BM_A and clearly legible through US. This demonstrates that BM_Z is opaque, BM_A translucent and US (moderately) transparent [26]. In addition, we can observe that the three samples are not colourless: BM_Z has a reddish colour, whereas BM_A and US are greyish.

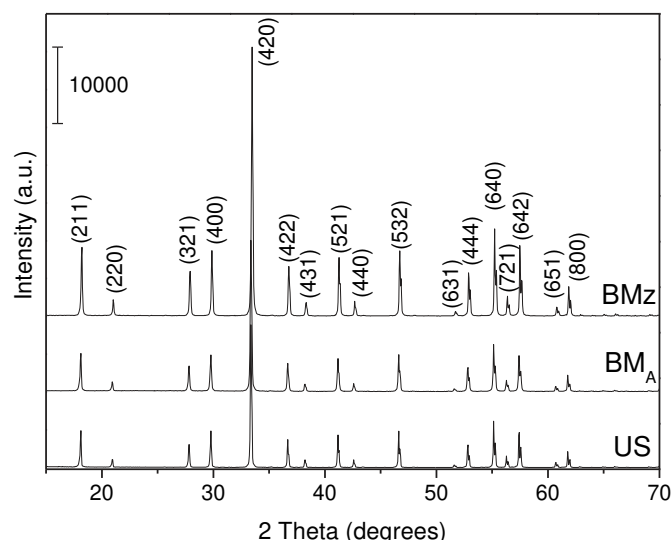
**Fig. 1.** Physical appearance of BM_Z (A), BM_A (B) and US (C) sintered materials.

The FE-SEM characterisation showed that the three materials were highly homogeneous and dense, independently from the dispersion route, as shown in [17] for the US and BM_A samples. US presented a mean grain size of 330 ± 50 nm with few residual pores, the size of which does not exceed 50 nm. For BM_A, a mean grain size of 360 ± 20 nm was estimated, with some small intragranular pores (<20 nm) as well as elongated intergranular ones (100–200 nm in size). Also BM_Z presented a very fine microstructure, with YAG grains of about 400 nm in size and very tiny (<50 nm) residual pores.

The three samples were submitted to XRD analysis, and the patterns (Fig. 2) were indexed as pure YAG phase (JCPDS 330040). Thus, if present, the amount of α -alumina or zirconia pollutants in BM powders was lower than the XRD detection limit.

Fig. 3 collects the Raman spectra of US, BM_Z and BM_A sintered materials in $400\text{--}1150\text{ cm}^{-1}$ range. With US, bands at 546, 692, 718, 783, 856 and 980 cm^{-1} are readily assigned to YAG, in agreement with the literature [27,28], in particular, the peak at 546 cm^{-1} can be assigned as the ν_2 (AlO_4) mode, whereas peaks at 692, 718, 783 and 856 cm^{-1} can be attributed to the ν_1 and ν_4 modes for the (AlO_4) unit.

Similar peaks were observed in the Raman spectrum of BM_Z, in which additional peaks at about 570 cm^{-1} and 594 cm^{-1} were also detected: they can be reasonably ascribed to yttria-stabilised zirconia vibrational modes. The latter assignment is supported by the fact that in tetragonal zirconia an intense band is generally observed at about 640 cm^{-1} , shifting to lower wavenumbers with increasing yttria content [29–31]. Thus, a limited yttrium diffusion within the zirconia lattice seems to take place during SPS process, up to the fully stabilisation of the cubic structure and the consequent formation of yttrium-depleted alumina particles inside the garnet matrix. The BM_A Raman spectrum is quite similar to that of US. The main difference lies in the slight signals, additional to those proper of YAG, observed at about 585 cm^{-1} and 625 cm^{-1} , which can be reasonably ascribed to α -alumina vibrational modes [32].

**Fig. 2.** XRD patterns of BM_Z, BM_A and US sintered materials.

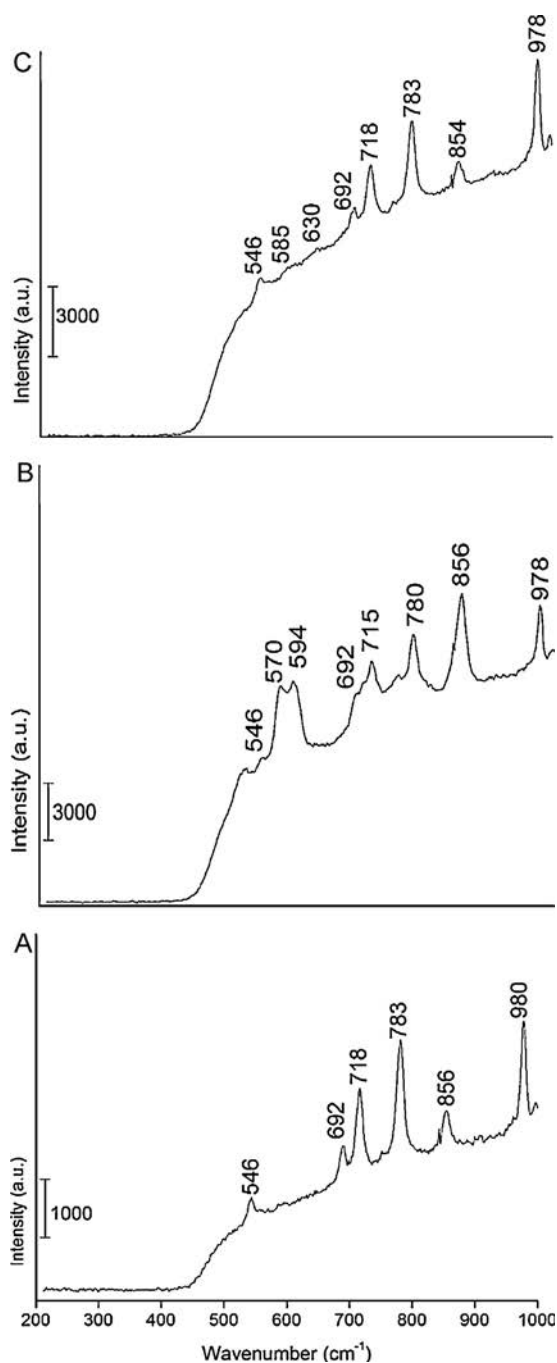


Fig. 3. Raman spectra of US (A), BM_Z (B) and BM_A (C) sintered materials.

Summarising, the different optical behaviour of the three samples can be explained according to their different fired density, pore size and phase purity. Zirconia and α -alumina debris in the BM materials will probably segregate at YAG grain boundaries, hindering densification and leaving large pores, as observed in BM_A. In a previous work [17], SEM observations coupled to EDX analyses performed on BM_A provided the presence of few grains with a darker phase contrast and a higher Al content as compared to the surrounding matrix. The presence of zirconia debris in BM_Z is further confirmed by the reddish colour of the sintered pellet. In fact, such a colour has been already observed in YSZ samples sintered at 1200 °C under vacuum for different times: samples became increasingly red in colour as the holding time increased [33]. The colour change (from white to reddish) was attributed to oxygen vacancies formed in the reducing atmosphere of the

sintering process. Accordingly, Penilla et al. [34] consolidated YAG powders, which were ball-milled with zirconia media, to translucency via SPS, and observed a red/brown colour which disappeared through annealing in air.

These observations agree with the current outcomes from Raman spectroscopy, and strengthen the hypothesis of a contamination of both BM_Z and BM_A from the milling media. The difference in refraction index between zirconia (2.15), alumina (1.76) and YAG (1.84) accounts for the lower transmittance in the milled samples. On the opposite, ultrasonication was found to be a very effective dispersion method, allowing to prepare fully dense, pure and optically transparent YAG materials.

3.2. Role of carbon contamination and/or oxygen vacancies on the optical properties of as-sintered and annealed US YAG

As-sintered US samples are greyish, as already observed for other SPS sintered oxides, ambiguously attributed in the literature to oxygen vacancies and/or to carbon contamination from the SPS equipment [14]. Jiang et al. [35] observed that the colour of sintered alumina samples became greyer as the sintering temperature increased, due to oxygen vacancies created in the reducing environment of the SPS chamber. Similarly, Zhang et al. [36] obtained yellowish-brown cubic-YSZ materials, which progressively darkened by increasing the SPS temperature. Grey colour and dark spots were also observed by Meir et al. in magnesium aluminate spinel [37], ascribed to carbon contamination from the SPS graphite dies. A further contribution is given by the work of Bernard-Granger et al. [13]: by means of optical microscopy, graphite particles of about 20 μ m in size, homogeneously dispersed inside a magnesium aluminate spinel matrix were observed, responsible for the dark/brown colour of the samples. In the case of YAG, Frage et al. [12] observed a higher optical transparency in LiF-doped materials, as compared to undoped ones. They demonstrated the effectiveness of this additive in reacting with the carbon contamination, removing it as volatile species and restoring the light transmittance. Finally, Lee et al. [38] reported a grey appearance for pressure-less, vacuum sintered YAG samples, supporting the hypothesis that oxygen vacancies rather than carbon contamination induced the darkening of the samples.

Here, as-sintered and annealed US pellets were submitted to XPS analysis and the resulting surface chemical compositions (at.%) are reported in Table 2: in all the samples, only Al, Y, O and C were detected. The presence of adventitious carbon due to surface contamination from atmosphere is usually observed in XP spectra; however, in the present case an additional contamination arising from the SPS equipment cannot be ruled out. The systematic decrease of C concentration with increasing annealing temperature supports the presence of graphite second-phase from the SPS die. In fact, a significant decrease of about 33% was detected after annealing at 600 °C, likely due to partial oxidation of surface carbon by air; further (moderate) decreases of about 4.3% and 6.2% were respectively determined after annealing at 900 °C and 1200 °C, with a final carbon content of about 27% at (Table 2). The corresponding C 1s XP spectra of US samples are reported in Fig. 4(a): both the as-sintered and annealed samples show a component peaking at ca. 285 eV, readily assigned to C–C and C–H

Table 2
Surface chemical composition (at.%) of as-sintered and annealed US samples, as obtained by XPS analysis.

Sample	Al (at.%)	Y (at.%)	O (at.%)	C (at.%)	Y/Al
US as-sintered	11.13	7.94	35.36	45.58	0.71
US annealed 600 °C	14.32	9.86	45.44	30.37	0.69
US annealed 900 °C	13.60	10.01	47.27	29.12	0.74
US annealed 1200 °C	14.38	9.81	48.51	27.30	0.68

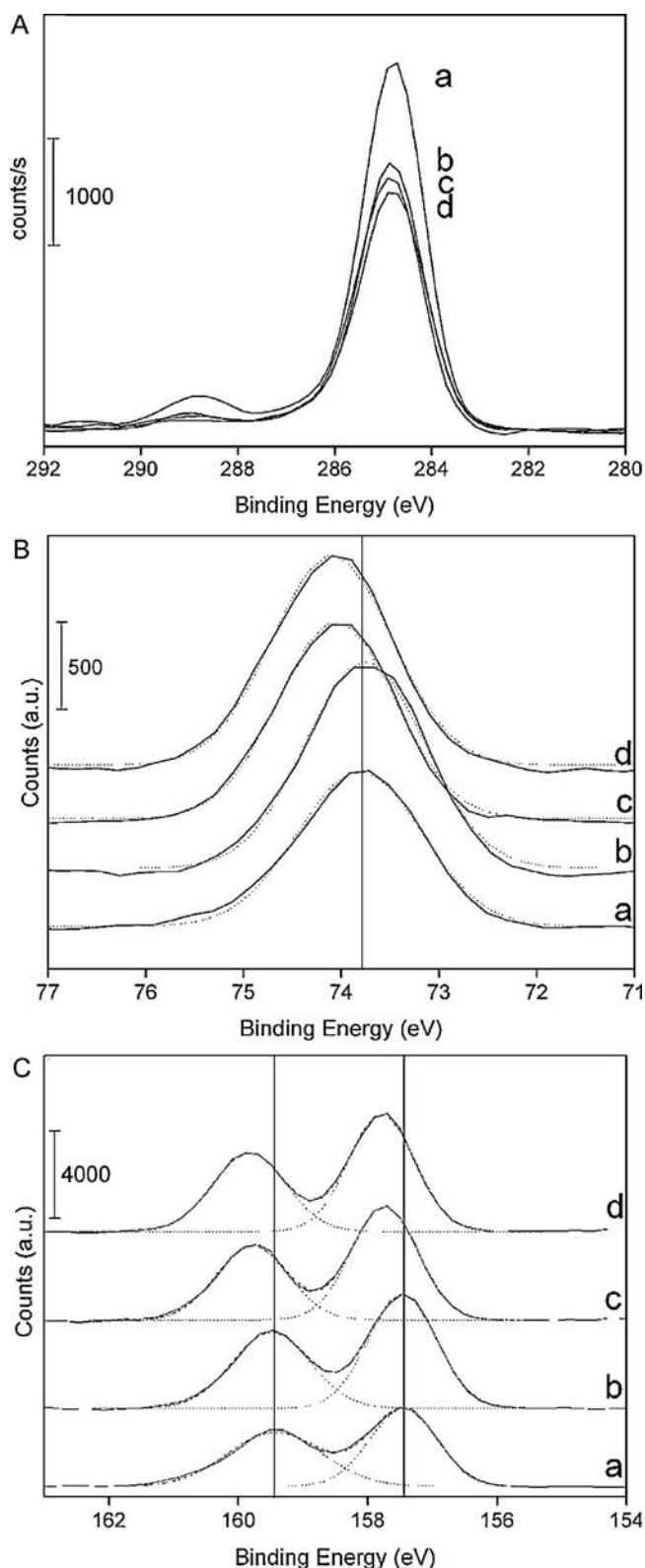


Fig. 4. High resolution XP spectra in the C 1s (A), Al 2p (B) and Y 3d (C) BE ranges, for as-sintered (a) and annealed at 600 °C (b), 900 °C (c) and 1200 °C (d) samples. Continuous line: original XP spectra; dotted lines: curve-fit results. The vertical lines in figures (B) and (C) underline the displacement at higher BEs for (c) and (d) samples.

groups [39]. In the as-sintered US, the component at higher binding energy (ca. 288 eV), is instead due to C atoms bonded to O [39], likely carbonates formed after exposure to atmospheres, and removed by annealing at higher temperatures.

Table 3

Results of curve-fits run on high-resolution XP spectra reported in Figs. 4 and 5.

Sample	Al 2p	Y 3d	O 1s
US as sintered	73.75	157.46	530.45
		159.49	532.15
			533.82
US annealed 600 °C	73.75	157.46	530.45
		159.49	532.15
			533.82
US annealed 900 °C	74.05	157.74	530.77
		159.78	532.31
			533.64
US annealed 1200 °C	74.09	157.78	530.79
		159.82	532.24
			533.50

The surface Y/Al atomic ratio was calculated for all the investigated materials, and collected in Table 2. Values range from 0.68 to 0.74, i.e. apparently higher than the stoichiometric ratio (0.60), but still within the experimental error.

Table 3 reports the most important features concerning XP spectra, whereas Fig. 4(b) and (c) report the Al 2p and the Y 3d XP spectra and related curve-fits for the as-sintered and annealed samples, whereas the related O 1s XP spectra are depicted in Fig. 5. For the as-sintered sample, the Al 2p peak is seen at 73.8 eV and the Y 3d one is split into two lines, Y 3d_{5/2}–Y 3d_{3/2}, due to spin–orbit interactions, respectively located at 157.4 and 159.4 eV [40]. From Table 3, we can observe quite similar binding energy values for the as-sintered and 600 °C-annealed material. On the opposite, a certain shift of binding energy from lower to higher values was observed for both Y 3d and Al 2p peaks in the 900 °C and 1200 °C-annealed samples. It has been reported that an increase of XPS binding energy of the core level usually indicates an increase of the positive charge of transition metal ions [41–43]. For instance, Hsieh et al. [43] observed a chemical shift from lower to higher binding energy for the Auger Zn LMM peak in ZnO films due to a decrease in the valence electron density and an increase in the oxidation state. Thus, the shift towards higher binding energy observed in our materials can be due to an increase in the number of oxygen atoms at the surface of annealed materials.

Curve of O1s XP spectra (Fig. 5) led to the identification of three components at 530.4 (O_I), 531.9 (O_{II}) and 533.4 eV (O_{III}), in good agreement with literature data [40,44]. The O_{III} peak is due to adsorbed O species (water, for instance) and will not be discussed further. The two peaks at lower binding energies were already been observed by Pawlak and co-workers [40] who showed that although the crystalline structure of YAG admits the presence of only type of oxygen ions, the O (1s) spectra of all the YAG systems exhibit two readily discernible peaks. An explanation for this dichotomy was discussed in the seminal paper by Pawlak et al. [40], involving for instance the different polarisation of oxygen valence electron density between aluminium and yttrium, since the Al–O bond has a higher covalent character with respect to the Y–O bond, and thus a higher binding energy. Fig. 6 displays the O 1s total area (O_I + O_{II} + O_{III}) as well as the ratio between the areas of O_I and O_{II} bands: in spite the continuous increase of the total Oxygen areas with the annealing temperature, an increase in the area ratio was observed up to 900 °C and then a decrease. As previously stated for other oxides [42,45] the O_{II} band could be also due to O atoms in oxygen deficient environment, i.e. close to oxygen vacancies. Therefore, variations in the intensity of O_{II} could be connected to changes in the concentration of oxygen vacancies occurring at the material surface. Such species seem to decrease in the present case as a consequence of the annealing in air at 600 °C and 900 °C, thanks to the reaction with air; the slight decrease in O_I/O_{II} areas ratio at 1200 °C could be reasonably due to some oxygen loss occurring at such a high temperature.

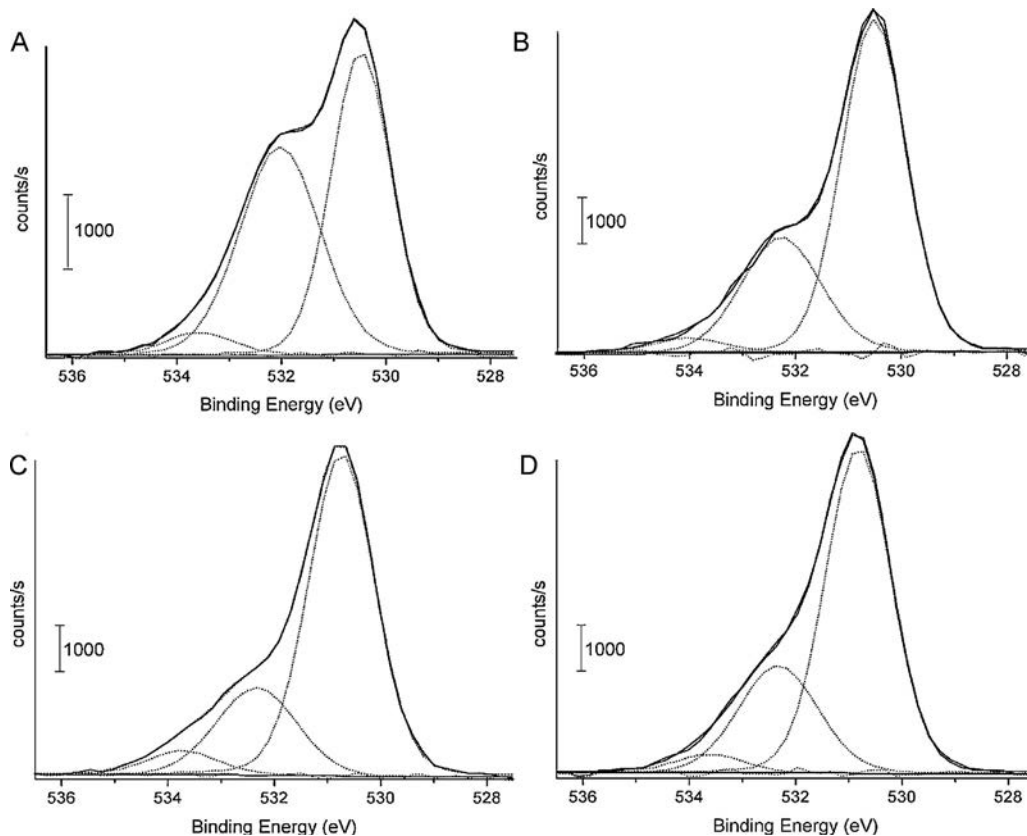


Fig. 5. High resolution XP spectra in the O 1s BE range for the as-sintered (a) and annealed at 600 °C (b), 900 °C (c) and 1200 °C (d) samples. Continuous line: original XP spectra; dotted lines: curve-fit results.

Annealing in air, carried out in a precise temperature range (namely, between 700 °C and 900 °C), was very effective in increasing the materials transparency. At the same time the samples progressively lightened, towards transparent and colourless materials.

For sake of clarity, Fig. 7(a) compares the transmittance curve of the as-sintered material with those of samples annealed at 600 °C, 900 °C and 975 °C for 1 h. The small leaps at about 850 nm are due to the different detectors used inside the spectrophotometer, as detailed in the Experimental section. The higher transmittance was reached after annealing at 900 °C; such behaviour can be explained on the ground of the XPS results, by assuming similar chemical features on the surface and in the bulk of the investigated materials. The results seem to indicate a slight increase of the

oxidation state and a decrease of the oxygen vacancies concentration occurring when the annealing temperature is increased up to 900 °C. In fact, at this temperature, either a shift of the Al 3p, Y 3d and O 1s towards (slightly) higher binding energy values and a decrease of the relative area of the O 1s component in the oxygen deficient region occur.

If the annealing temperature further increased (for instance, up to 975 °C, as shown in Fig. 7(a) the transmittance at low wavelengths decreased again. Transmittance in the infrared range, on the opposite, was increased for all the investigated annealing temperatures. It was supposed that such annealing conditions, carried out at a low heating rate (10 °C/min) and for a prolonged heating time (1 h) as compared to the SPS conditions in that temperature range, could promote microstructural changes, as well as coalescence of colour centres and tiny pores leading to new or larger defects, as already reported by Zhang et al. [46].

To explain the results we have to consider that transmittance is affected by both absorption (from colour centres, i.e. oxygen vacancies with trapped electrons) and scattering (mainly due to pores) phenomena, which can be differently affected by the annealing process. Upon annealing, the absorption coefficient is reduced, due to back-diffusion of oxygen which reduces the concentration of colour centres. However, over a “critical” annealing temperature, the scattering coefficient owing to the increased porosity amount and size [46] increases. In this condition, residual pores dominate the transparency of the annealed specimens, since most colour centres have been removed and eventually converted into pores.

Our results also show that the materials transparency (in the visible range) is not significantly affected by the carbon contamination from the SPS equipment. In fact, from Fig. 7(a) we can observe that the transmittance curves for the as-sintered

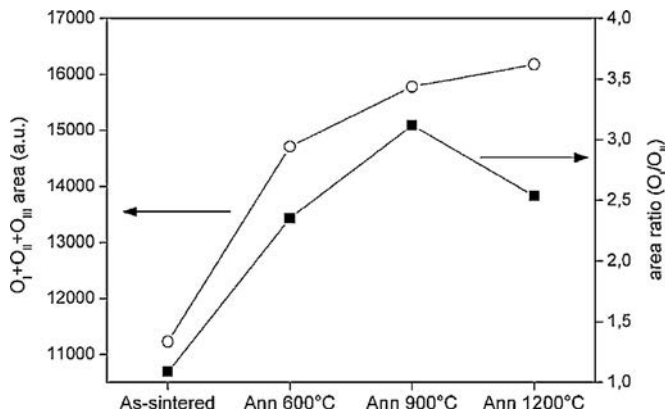


Fig. 6. Evolution of the O 1s total area (circles) and of O_I/O_{II} areas ratio (squares).

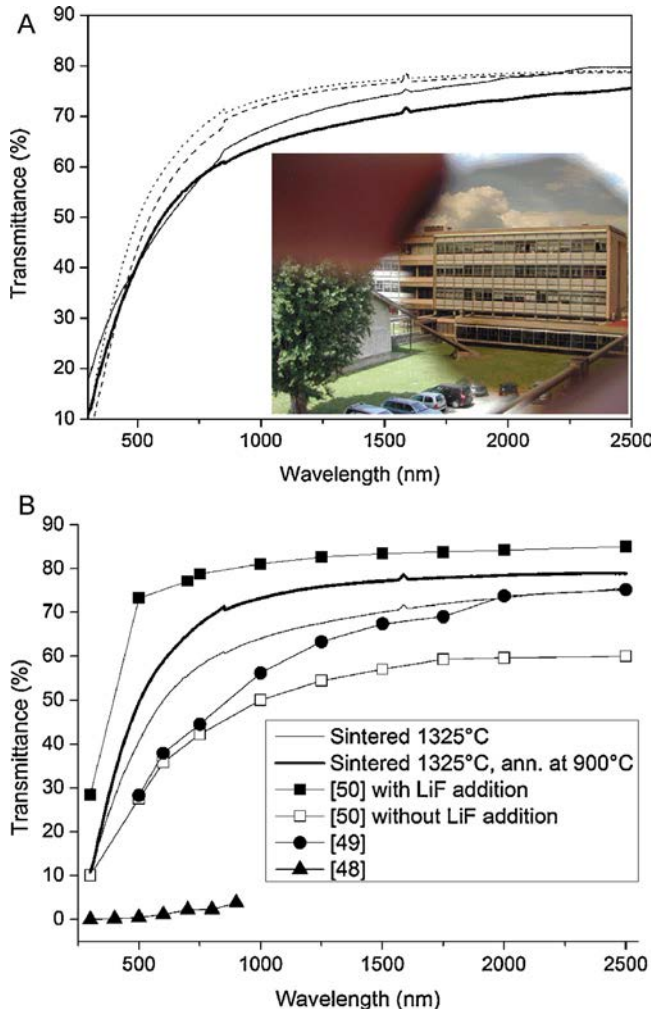


Fig. 7. (a) YAG transmittance of for the as-sintered (solid thick line) and annealed at 600 °C (solid thin line), 900 °C (dotted line) and 975 °C (dashed line) samples. Inset the figure, a high distance image, as observed through the sample sintered at 1325 °C, here before annealing; (b) comparison with previous studies of SPS sintered YAG.

and 600 °C-annealed materials are quite superimposable (up to about 800 nm), in spite of the strong decrease of the carbon concentration after annealing at 600 °C. Inset to Fig. 7(a), a highly detailed image observed at a significant distance through a sample sintered at 1325 °C (here before annealing and with a thickness of 2.2 mm), attesting the good transparency of the specimen. In Fig. 7(b) the transmittance of this material is compared with the already published results on YAG fabricated by SPS, after proper scaling for thickness (1.5 mm). It is shown that the transmittance here reached is higher than the one previously obtained for YAG sintered without any additive [12,47,48], even if still lower than the one of YAG sintered with LiF doping [12].

3.3. Microstructural and mechanical characterisation of US samples

The basic mechanical properties of the US samples were determined as a function of the sintering temperature. Table 4 collects the fired density of the materials, showing that the theoretical density was reached for temperatures higher than 1325 °C.

Fig. 8 shows the microstructure of US YAG materials, sintered in the range 1250–1400 °C. Highly homogeneous microstructures were observed for materials sintered up to 1375 °C, with a very narrow distribution of YAG grain size around its average value. The 1250 °C and 1300 °C-sintered pellets were characterised by rounded grains, attesting the incomplete densification of the materials. At higher temperatures the grain morphology changed to well-faceted grains and equiaxed polyhedral-shaped grains were observed in the material sintered at 1400 °C. In this last sample, a significant grain growth occurred, giving rise to inhomogeneous microstructures, in which some abnormally grown grains were observed. In all the microstructures, few residual pores were observed, as already stated in literature for spark plasma sintered materials. In fact, Chaim et al. [47] carried out extensive studies on the densification mechanism of YAG and other oxides by SPS, concluding that with increasing grain size, the complete elimination of the residual close pores is not achievable and their presence is an inevitable feature on the resulting microstructure. In addition, when the sintering temperature increases, the pore size also increases due to pore coalescence phenomena [36,46,47]. This is put in evidence by the arrows in Fig. 8, showing larger pores in the coarsened microstructures. Such a feature agrees with the transmittance data collected in Table 4: the higher values were recorded for the samples sintered at 1325 °C and 1350 °C, which benefit of nearly full densities and ultra-fine microstructures. For better comparing the transmittance data, values in Table 4 are referred to sintered materials, but not submitted to any annealing treatment.

Fig. 9 displays the average grain size, the Vickers hardness and the fracture toughness as a function of the sintering temperature.

We can observe high hardness values for all samples sintered in the 1250–1350 °C range, as a result of their nearly theoretical density and ultra-fine grain size. On the opposite, an abrupt decrease of the Vickers hardness was observed for the 1375 °C and 1400 °C SPS-processed materials, due to their coarsened microstructures. The less homogeneous microstructure of the 1400 °C-sintered sample accounts for the larger standard deviation of the estimated data.

Samples sintered at 1300–1325 °C presented a very high hardness of about 16.5–17.0 GPa. As a comparison, a hardness value of 18 GPa (under 2 N load) for a micronic-sized, translucent YAG, doped with various amounts of either SiO₂ or MgO, was found [49]; Frage et al. [16] determined a maximum hardness of 1570 HV for a fine-grained Nd-doped YAG ($\approx 0.5 \mu\text{m}$) under an applied load of 0.3 kg; a lower value of 1500 HV, under the same 0.3 kg load, was determined by Mezeix and Green [2] for a micronic-sized material; finally an average Vickers hardness of 12.5 GPa was determined by Li et al. [50] for a sintered YAG whose grain size was about 15 μm .

Table 4

Fired density, average grain size, RIT, Vickers hardness and fracture toughness for US YAG sintered in the 1250–1400 °C range (un-annealed materials).

Sintering temperature (°C)	Fired density (%TD)	Grain size (μm)	RIT (%) 1 mm thickness, ± 0.5	HV (GPa)	K_{IC} (MPa m ^{1/2})
1250	99.50	0.20 ± 0.06	n.d.	16.1 ± 0.7	1.26 ± 0.12
1300	99.84	0.26 ± 0.05	26.5	17.1 ± 1.0	1.56 ± 1.15
1325	99.99	0.33 ± 0.05	60.0	16.7 ± 1.4	1.91 ± 1.20
1350	99.99	0.61 ± 0.1	54.0	15.8 ± 0.7	1.35 ± 0.15
1375	99.99	2.72 ± 0.91	n.d.	13.3 ± 1.1	1.61 ± 0.18
1400	99.99	9.79 ± 1.89	23.3	11.8 ± 1.9	1.15 ± 0.16

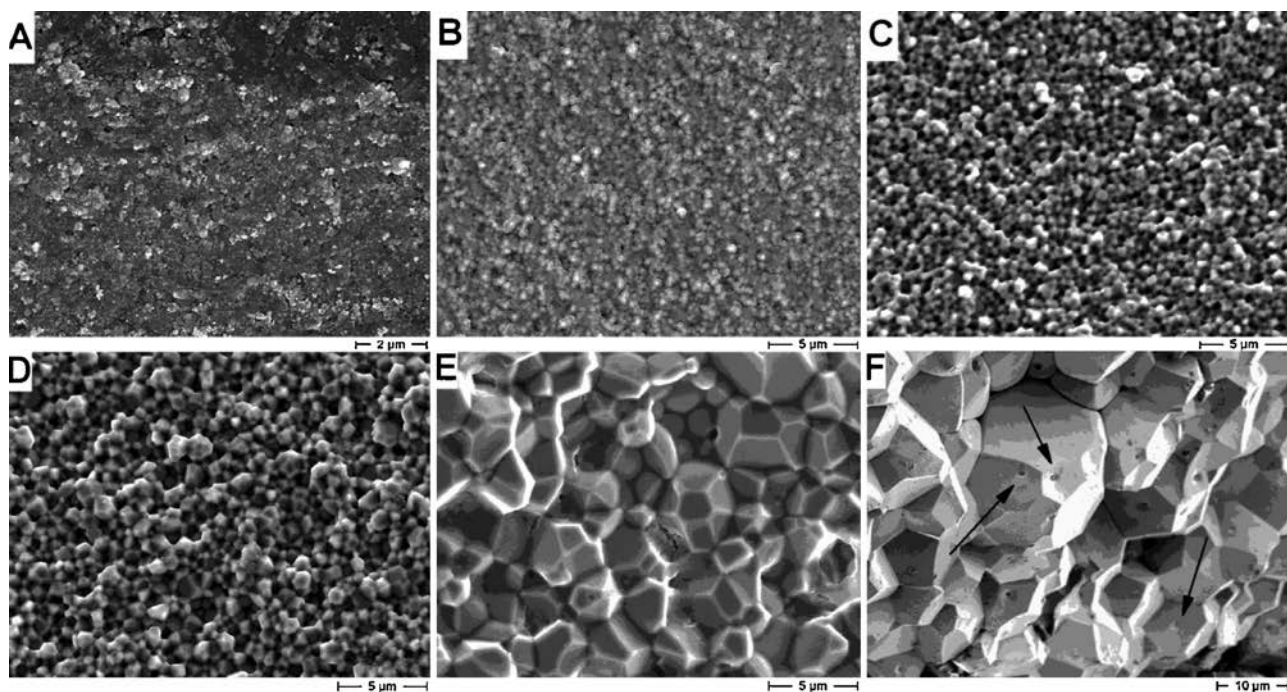


Fig. 8. FESEM micrographs of US YAG spark plasma sintered at (a) 1250 °C; (b) 1300 °C; (c) 1325 °C; (d) 1350 °C; (e) 1375 °C and (f) 1400 °C.

In addition, hardness is significantly higher than that of YAG single crystal (ranging from 12.8 to 13.5 GPa [2]), supporting the interest in the polycrystalline material over YAG single crystal in applications which require both good optical and mechanical properties.

The crack indentation technique was here used to estimate the fracture toughness. From Vickers indentations, two main types of crack can propagate, precisely classic median/radial “half-penny” cracks and “Palmqvist” cracks [51]. There has been much discussion concerning the methods used to differentiate half-penny and Palmqvist cracking systems. By just using the surface of the crack system as a guide, the crack type can be distinguished by the ratio of the crack length from the centre to the diameter of the indent (c/a). A generally accepted criterion is that if $c/a \geq 2$, then the cracking is half-penny, and if $c/a < 2$, the cracking is Palmqvist [52]. In our case c/a ranged from 2.8 to 3.6, depending on the sintering temperature. So, fracture toughness was here determined by using the Anstis formula [24] which applies to the half-penny

cracks. The K_{IC} values vs. sintering temperature are shown Fig. 9: values range from 1.1 to 1.8 $\text{MPa m}^{1/2}$ and a clear dependence on the microstructure cannot be established. Thus, moderate toughness values were here determined but in agreement with literature data. In fact, K_{IC} of 1.61 $\text{MPa m}^{1/2}$ was determined by Mezeix and Green [2]; a value of 1.7 $\text{MPa m}^{1/2}$ was found by De With and Parren [49] and a slightly higher value of 2.2 $\text{MPa m}^{1/2}$ was found by Boniecki et al. [52], determined by three or four-points bending strength on notched bars; finally a value of 2.2 $\text{MPa m}^{1/2}$ was found by Li et al. [45] by crack indentation technique, by using the equation given by Niihara [53] for $0.25 \leq l/a \leq 2.5$. For a comparison, when the same formula is applied to our materials, fracture toughness values ranging from 2.1 to 2.6 $\text{MPa m}^{1/2}$ were determined.

4. Conclusions

This work demonstrates the key role of the dispersion process on YAG optical properties. YAG powders, synthesised by reverse-strike co-precipitation, were calcined at 1000 °C and dispersed by either ball-milling (BM) or ultrasonication (US). After consolidation by SPS to nearly theoretical density, only the US powder gave rise to a transparent material (transmittance of about 60% at 600 nm, for 1 mm thickness). Raman spectroscopy showed the occurrence of some contamination in the BM materials due to the milling media (precisely, α -alumina and zirconia debris) not detectable by XRD analysis.

Annealing in air was highly effective in increasing the materials optical properties. In fact, the as-sintered material presented a greyish colour, which lightened during subsequent annealing in air, and the light transmittance progressively increased.

The increase in transparency was, however, reached only when annealing was carried out in quite narrow temperature range, between about 700 °C and 900 °C. XPS results indicated that, in this temperature range, a certain increase in number of oxygen atoms and restoration of oxygen vacancies occurred. Some oxygen vacancies were reasonably produced during the SPS process under a reducing environment, and affected the material transparency

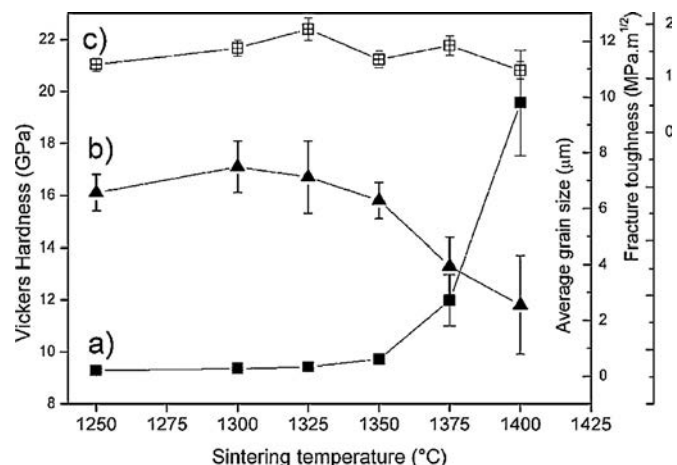


Fig. 9. Average grain size (a), Vickers hardness (b) and fracture toughness (c) of US YAG as a function of the spark plasma sintering temperature.

due to light absorbance phenomena. At lower temperature, the oxygen vacancies restoration process was not complete, whereas at higher temperature a possible change of the microstructural features (i.e. coalescence of tiny pores in larger ones) reduced the optical transparency of the materials due to scattering phenomena.

The carbon contamination, a common drawback of the SPS process, seems not to relevantly affect the materials transparency. In fact, in spite of the strong reduction of the C (surface) concentration after annealing at 600 °C, a corresponding increase of light transmittance in the visible range was not observed.

Finally, fully dense, fine-grained materials, as YAG sintered at 1300–1350 °C, were characterised by a very high hardness. This demonstrates that SPS is a powerful tool to tailor the final microstructure and related properties, and supporting the interest in the polycrystalline YAG over the single crystal for applications in which both good mechanical and optical properties are required.

References

- [1] T.A. Parthasarathy, T. Mah, K. Keller, *Ceram. Eng. Sci. Proc.* 12 (1991) 1767–1773.
- [2] L. Mezeix, D. Green, *Int. J. Appl. Ceram. Technol.* 3 (2006) 166–176.
- [3] P. Palmero, G. Fantozzi, F. Lomello, G. Bonnefont, L. Montanaro, *Ceram. Int.* 38 (2012) 433–441.
- [4] V. Naglieri, P. Palmero, L. Montanaro, *J. Therm. Anal. Calorim.* 97 (2009) 231–237.
- [5] P. Palmero, A. Sola, V. Naglieri, D. Bellucci, M. Lombardi, V. Cannillo, *J. Mater. Sci.* 47 (2012) 1077–1084.
- [6] P. Palmero, V. Naglieri, G. Spina, M. Lombardi, *Ceram. Int.* 37 (2011) 139–144.
- [7] G.C. Wei, *J. Phys. D: Appl. Phys.* 38 (2005) 3057–3065.
- [8] Y. Li, S. Zhou, H. Lin, X. Hou, W. Li, H. Teng, T. Jia, *J. Alloys Comp.* 502 (2010) 225–230.
- [9] A. Krell, T. Hutzler, J. Kinke, *J. Eur. Ceram. Soc.* 29 (2009) 207–221.
- [10] H. Yagi, T. Yanagitani, T. Numazawa, K. Ueda, *Ceram. Int.* 33 (2007) 711–714.
- [11] S.F. Wang, J. Zhang, D.W. Luo, F. Gua, D.Y. Tang, Z.L. Dong, G.E.B. Tan, W.X. Que, T.S. Zhang, S. Li, L.B. Kong, *Prog. Solid State Chem.* 41 (2013) 20–54.
- [12] N. Frage, S. Kalabukhov, N. Sverdlov, V. Ezersky, M.P. Dariel, *J. Eur. Ceram. Soc.* 30 (2010) 3331–3337.
- [13] G. Bernard-Granger, N. Benameur, C. Guizarda, M. Nygren, *Scripta Mater.* 60 (2009) 164–167.
- [14] P. Fu, W. Lu, W. Lei, Y. Xu, X. Wang, J. Wu, *Ceram. Int.* 39 (2013) 2481–2487.
- [15] B.N. Kim, K. Morita, J.H. Lim, K. Hiraga, H. Yoshida, *J. Am. Ceram. Soc.* 93 (2010) 2158–2160.
- [16] N. Frage, S. Kalabukhov, N. Sverdlov, V. Kasiyan, A. Rothman, M.P. Dariel, *Ceram. Int.* 38 (2012) 5513–5519.
- [17] G. Spina, G. Bonnefont, P. Palmero, G. Fantozzi, J. Chevalier, L. Montanaro, *J. Eur. Ceram. Soc.* 32 (2012) 2957–2964.
- [18] X. Wang, R. Zheng, Z. Liu, H. Ho, J. Xu, S.P. Ringer, *Nanotechnology* 19 (2008) 1–8.
- [19] P. Palmero, C. Esnouf, L. Montanaro, G. Fantozzi, *J. Eur. Ceram. Soc.* 25 (2005) 1565–1573.
- [20] P. Palmero, A. Simone, C. Esnouf, G. Fantozzi, L. Montanaro, *J. Eur. Ceram. Soc.* 26 (2006) 941–947.
- [21] P. Palmero, L. Montanaro, *J. Therm. Anal. Calorim.* 88 (2007) 261–267.
- [22] P. Palmero, M. Lombardi, L. Montanaro, M. Azar, J. Chevalier, V. Garnier, G. Fantozzi, *Int. J. Appl. Ceram. Technol.* 6 (2009) 420–430.
- [23] G.D. Quinn, P.J. Patel, I. Lloyd, *J. Res. Natl. Inst. Stand. Technol.* 107 (2002) 299–306.
- [24] G. Anstis, P. Chantikul, B. Lawn, *J. Am. Ceram. Soc.* 64 (1981) 533–538.
- [25] V. Cannillo, P. Palmero, T. Manfredini, L. Montanaro, *Int. J. Mater. Prod. Technol.* 35 (2009) 392–406.
- [26] A. Krell, P. Blank, H. Ma, T. Hutzler, M.P.B. van Bruggen, R. Apetz, *J. Am. Ceram. Soc.* 86 (2003) 12–18.
- [27] Y.F. Chen, P.K. Lim, S.J. Lim, Y.J. Yang, L.J. Hu, H.P. Chiang, W.S. Tse1, J. Raman Spectrosc. 34 (2003) 882–885.
- [28] A. Lukowiak, R.J. Wiglus, M. Maczka, P. Gluchowski, W. Strek, *Chem. Phys. Lett.* 494 (2010) 279–283.
- [29] W.C. Jung, J.L. Hertz, H.L. Tuller, *Acta Mater.* 57 (2009) 1399–1404.
- [30] A. Ghosh, A.K. Suri, M. Pandey, S. Thomas, T.R. Rama Mohan, B.T. Rao, *Mater. Lett.* 60 (2006) 1170–1173.
- [31] J.M. Calderon-Moreno, M. Yoshimura, *Solid State Ionics* 154/155 (2002) 125–133.
- [32] A. Misra, H.D. Bist, M.S. Navati, R.K. Thareja, J. Narayan, *Mater. Sci. Eng. B* 79 (2001) 49–54.
- [33] S. Casolco, J. Xu, J.E. Garay, *Scripta Mater.* 58 (2008) 516–519.
- [34] E.H. Penilla, Y. Kodera, J.E. Garay, *Mater. Sci. Eng. B* 177 (2012) 1178–1187.
- [35] D.T. Jiang, D.M. Hulbert, U. Anselmi-Tamburini, T. TNg, D. Land, A.K. Mukherjee, *J. Am. Ceram. Soc.* 91 (2008) 151–154.
- [36] H. Zhang, B.-N. Kim, K. Morita, H. Yoshida, K. Hiraga, Y. Sakka, *Sci. Technol. Adv. Mater.* 12 (2011) 1–6.
- [37] S. Meir, S. Kalabukhov, N. Froumin, M.P. Dariel, N. Frage, *J. Am. Ceram. Soc.* 92 (2009) 358–364.
- [38] S.-H. Lee, S. Kochawattana, G.L. Messing, *J. Am. Ceram. Soc.* 89 (2006) 1945–1950.
- [39] M.G. Faga, A. Vallée, A. Bellosi, M. Mazzocchi, N.N. Thinh, G. Martra, S. Coluccia, *J. Eur. Ceram. Soc.* 32 (2012) 2113–2120.
- [40] D.A. Pawlak, K. Wozniak, Z. Frukacz, T.L. Barr, D. Fiorentino, S. Seal, *J. Phys. Chem. B* 103 (1999) 1454–1461.
- [41] M.T. Greiner, L. Chai, M.G. Helander, W.-M. Tang, Z.-H. Lu, *Adv. Funct. Mater.* 22 (2012) 4557–4568.
- [42] Q.-H. Wu, A. Thissen, W. Jaegermann, M. Liu, *Appl. Surf. Sci.* 236 (2004) 473–478.
- [43] P.T. Hsieh, Y.C. Chen, K.S. Kao, C.M. Wang, *Appl. Phys. A* 90 (2008) 317–321.
- [44] M. Kruczek, E. Talik, H. Sakowska, M. Gała, M. Świrkowicz, *Cryst. Res. Technol.* 40 (2005) 439–443.
- [45] X. Li, Y. Wang, W. Liu, G. Jiang, C. Zhu, *Mater. Lett.* 85 (2012) 25–28.
- [46] H. Zhang, B.-N. Kim, K. Morita, H. Yoshida, J.-H. Lim, K. Hiraga, *J. Am. Ceram. Soc.* 94 (2011) 2981–2986.
- [47] R. Chaim, M. Kalina, J.Z. Shen, *J. Eur. Ceram. Soc.* 27 (2007) 3331–3337.
- [48] M. Suarez, A. Fernandez, J.L. Menéndez, R. Torrecillas, *J. Alloys Compd.* 493 (2010) 391–395.
- [49] G. De With, J.E.D. Parren, *Solid State Ionics* 16 (1985) 87–93.
- [50] J. Li, Y. Wu, Y. Pan, W. Liu, L. Huang, J. Guo, *Opt. Mater.* 31 (2008) 6–17.
- [51] C.B. Ponton, R.D. Rawlings, *Mater. Sci. Technol.* 5 (1989) 865–871.
- [52] M. Boniecki, Z. Librant, A. Wajler, W. Wesolowski, H. Węglarz, *Ceram. Int.* 38 (2012) 4517–4524.
- [53] K. Niihara, R. Morena, D.P.H. Hasselman, *J. Mater. Sci. Lett.* 1 (1982) 13.